Germanium vertically light-emitting micro-gears generating orbital angular momentum

Abdelrahman Z. Al-Attili,[1,*] Daniel Burt,[1] Zuo Li,[1], Naoki Higashitarumizu,[2] Frederic Y. Gardes,[1] Katsuya Oda,[3] Yasuhiko Ishikawa,[2] and Shinichi Saito[2,*]

[1] *Sustainable Electronic Technologies, Electronics & Computer Science, University of Southampton, SO17 1BJ, UK*

[2] *Department of Electrical and Electronic Information Engineering, Toyohashi University of Technology, 1-1 Hibarigaoka, Tempaku, Toyohashi 441-8580, Japan*

[3] *Research & Development Group, Hitachi, Ltd., 1-280 Higashi-Koigakubo, Kokubunji, Tokyo 185-8601, Japan*

[*] *AbdAttili@ieee.org, S.Saito@soton.ac.uk*

Abstract: Germanium (Ge) is capturing researchers'interest as a possible optical gain medium implementable on Complementary Metal-Oxide-Semiconductor (CMOS) chips. Band-gap engineering techniques, relying mainly on tensile strain, are required to overcome the indirect band-gap nature of bulk Ge and promote electrons injection into the direct-gap valleys. We used Ge-on-SOI wafers with a high-crystalline-quality Ge layer to fabricate Ge micro-gears on Silicon (Si) pillars. Micro-gears are created by etching a periodic grating-like pattern on the circumference of a conventional micro-disk, resulting in a gear shape. Thermal built-in stresses within the SiO_2 layers that encapsulate the micro-gears were used to impose tensile strain on Ge. Biaxial tensile strain values ranging from 0.3-0.5% are estimated based on Raman spectroscopy measurements and Finite-Element Method (FEM) simulations. Multiple sharp-peak resonances within the Ge direct-gap were detected at room temperature by Photo-Luminescence (PL) measurements. Investigating the micro-gears spectrum using Finite-Difference Time-Domain (FDTD) simulations, we identified vertically emitted optical modes with non-zero Orbital Angular Momentum (OAM).

© 2018 Optical Society of America under the terms of the OSA Open Access Publishing Agreement

1. Introduction

The rapid progress towards the convergence of electronics and photonics on a Complementary Metal-Oxide-Semiconductor (CMOS) platform is motivating the development of a Silicon (Si)-compatible laser source [1–4]. Being the last component to be yet created, this monolithic light source has well-defined criteria to meet [5, 6]. The fact that, other necessary optical-circuitry components such as modulators [7], waveguides [8] and photodetectors [9–11], are well established. For instance, some of the requirements to be met are compatibility with CMOS production lines [1, 2], acceptable threshold and power consumption [5, 6], in addition to having a suitable emission wavelength permitting signal transmission and manipulation on a Si-based platform [1, 2]. Accordingly, germanium (Ge) is considered a highly possible candidate [1–5, 12].

Ge is a group IV element that is already established within the CMOS industry, in fact it is used in the source and drain in some MOS Field-Effect-Transistors (MOSFETs) generations [12]. It also has a unique band-gap that can be engineered to provide direct-gap optical gain [1–4]. This arises from the small energy difference of 0.136 eV between its direct (Γ) and indirect (L) conduction band (CB) valleys, and their corresponding deformation potentials [13–15]. Hence, band-gap engineering of Ge relies mainly on tensile strain to minimize or even eliminate this energy difference between Γ and L CB valleys [16, 17]. This leads to an enhanced probability of

electrons injection into the direct Γ valleys, consequently increasing the efficiency of radiative recombinations [15–17]. *n*-type doping is also suggested to fill the indirect L valleys with electrons, reducing the injection requirements to achieve transparency [16–18]. A tensile strain of approximately 2% is expected to convert Ge into a direct gap material [13–17, 19]. In fact, several reports of Ge optical gain [20, 21] and lasing [22–26] have emerged during the last decade.

The first optical gain [20], optically-pumped [22] and electrically-pumped [24] Ge lasing reports relied on the inherent thermal tensile strain of approximately 0.2% within Ge films grown on Si [27]. Yet, high lasing threshold directed subsequent research efforts towards utilizing higher tensile strain values [2, 15, 17, 19]. Researchers have reported multiple techniques for this purpose [2]. The use of stressor layers [19, 26, 28–32] and fabricating freestanding structures [33, 34] are very common approaches. Namely, the use of initially compressively-stressed Si_xN_y stress liners have been very popular across the Ge community [2, 19, 26, 29–32, 35–37]. Stress liners on top [35], top and bottom [26], and all-around [32, 37] Ge structures have been investigated. All-around coverage results in higher tensile strain values and enhances the homogeneity compared to one-sided coverage, as the Ge structures get stretched in all directions [19, 26, 32, 37]. All-around coverage of Ge micro-disks [19, 26, 32] and rings [37] were demonstrated. Tensile strain values up to approximately 2% were achieved resulting in a direct-gap Ge [19]. However, room temperature lasing of Ge micro-disks or rings have not been reported yet.

Although current research efforts are focusing on realizing Ge lasing with a reduced lasing threshold compared to existing reports [22–26], other device requirements must be considered for a practical implementation within Si chips, such as coupling to an optical interconnect system [1, 6]. Considering the proposed future outlook of optical communications [6, 38], vertical emission of a Ge laser source is advantageous, especially for on-board and chip-to-chip communications, which would rely on vertical exchange of data between CMOS chips and electronic boards with embedded waveguides [38]. Vertical coupling of optical signals can be achieved using several coupling techniques, for example, adiabatic coupling [38] and grating couplers [38, 39]. Such techniques permit emitting the laser signal in-plane, yet requires a dedicated optical component for vertical coupling. On the other hand, this can also be achieved directly by vertical emission of optical signals from the laser cavity, as the case in Vertical-Cavity Surface-Emitting Lasers (VCSELs) [40].

In this paper, we demonstrate fabricating Ge micro-gears on Si pillars (Fig. 1) with an all-around SiO_2 stressor for vertical emission of direct-gap resonances. Micro-gears are fabricated by etching periodic slits around a conventional micro-disk structure. Such structures have been introduced before to reduce lasing threshold compared to micro-disks, explained by enhancing the Purcell effect [41, 42]. A sufficient representation of micro-gears and their characteristics can be found in literature [41, 42]. We exploit inherent thermal stresses within the buried-oxide layer (BOX) in Ge-on-SOI wafers, along with plasma-enhanced chemical-vapor deposition (PECVD) SiO_2 capping layer, as a source of tensile strain. Accumulation of tensile strain within the Ge structures is predicted using finite-element method (FEM) simulations, providing a three-dimensional visualization of the resulting strain distribution. Experimental tensile strain values were measured using Raman spectroscopy. Photo-Luminescence (PL) spectra with sharp-peak direct-gap resonances were measured from micro-gears at room temperature. Using Finite-Deference Time-Domain (FDTD) simulations we confirmed the emission of certain modes vertically out-of-plane, by monitoring the fields above the gear surface and calculating far-field projections. Further investigation of mode profiles and phase fronts, we observed the generation of orbital angular momentum (OAM) at certain resonant wavelengths. Resonant modes with OAM numbers of 0, 1 and 2 were clearly identified.

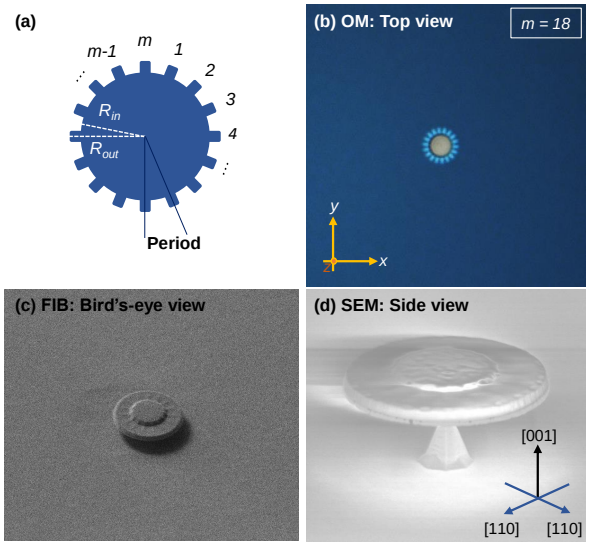

Fig. 1. Ge micro-gears. (a) Top-view sketch of a micro-gear structure showing the design parameters, namely the inner radius (R_{in}), outer radius (R_{out}) and the number of periods (m). (b) Optical Microscopy (OM) image of a Ge micro-gear after dry-etching. A visible optical mode is seen in the gears region. (c) Focused-Ion Beam (FIB) image showing birds-eye view of a Ge micro-gear encapsulated by buried (bottom) and PECVD (top) SiO_2 on a Si pillar. (d) Scanning-Electron Microscopy (SEM) side-view of a Ge micro-gear. The pyramidal shape of the Si pillar is obvious due to anisotropic TMAH etching. Crystallographic directions of the wafer are annotated on the bottom left corner.

2. Device structure and fabrication

We used Ge-on-SOI wafer with a stack of 200 nm Ge, 20 nm SOI and 145-nm-thick BOX to fabricate Ge micro-gears on Si pillars as shown in Fig. 1. Design parameters, namely, the inner radius (R_{in}), outer radius (R_{out}), gear depth given by the difference between them ($R_{out} - R_{in}$), and the number of gear periods (m), are shown in Fig. 1(a). Figures 1(b)-1(d) show examples of the devices using optical microscopy (OM), focused-ion beam (FIB), and scanning-electron microscopy (SEM), respectively. Fabrication process starts with wafers cleaning, which is done using subsequent steps of hydrofluoric (HF) and hydrochloric (HCl) acids (Fig. 2(a)). This is done prior to micro-gears patterning using electron-beam lithography. The Ge layer is then dry etched into micro-gears by reactive-ion etching (RIE) (Fig. 2(b)). Micro-gears with an outer radius (R_{out}) of 1-2 μm (outer diameter $2R_{out}$ = 2-4 μm), gear depth ($R_{out} - R_{in}$) of 50-500 nm, and total number of periods (m) ranging from 14 to 21 were fabricated. Dry-etching is extended downwards to remove the exposed SOI layer below Ge and then stopped at the top BOX surface (Fig. 2(b)).

A 200-nm-thick PECVD SiO_2 capping layer was then deposited on top at 350 °C (Fig. 2(c)). This layer serves as a passivation layer containing the Ge micro-gear and protecting it from the subsequent wet etching steps. The thickness and deposition conditions of this layer have been chosen carefully to satisfy two requirements: firstly, ensure a symmetrical stack of SiO_2 below and above the Ge-on-SOI layer for maximum modal confinement, due to the higher effective refractive index expected in the case of stack symmetry [43]. This was done assuming that the 20-nm-thick SOI

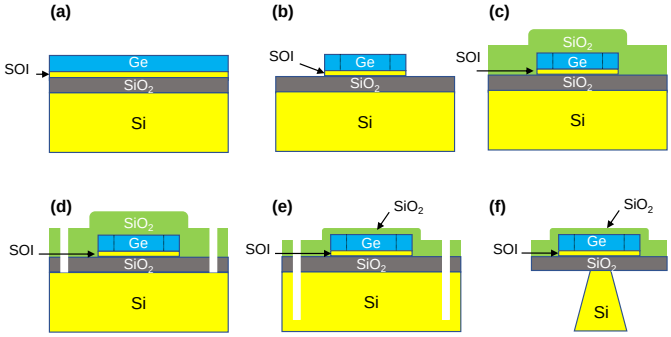

Fig. 2. Fabrication process of Ge micro-gears on Si pillars. (a) Cleaning of Ge-on-SOI wafers using HF and HCl acids. (b) Dry-etching of Ge-on-SOI micro-gears patterned with electron-beam lithography with different designs. (c) Deposition of PECVD SiO_2 layer to protect Ge and SOI from the following steps and impose tensile strain on Ge. (d) Dry-etching of SiO_2 to form a disk structure surrounding the Ge micro-gear. (e) Inductively-coupled plasma (ICP) dry-etching of bulk Si to form a 1-μm-high pedestal, followed by (f) TMAH etching of bulk Si to form a pyramidal-shaped pillar.

layer has a negligible effect on the effective refractive index of the optical modes [43]. Secondly, impose a suitable tensile-strain on the Ge micro-gear. The PECVD SiO_2 layer was then patterned into micro-disks encapsulating the Ge gears by RIE down to the handle Si wafer (Fig. 2(d)). The SiO_2 disks are concentric with the Ge gears with a radius of R_{out} + 400 nm to allow for alignment tolerances. Another dry-etching step was used to form a Si pedestal, using the top PECVD SiO_2 as a hard mask (Fig. 2(e)). Inductively-coupled plasma (ICP) etching with a remarkable selectivity of 20:1 (Si:SiO_2) permitted etching down to 1 μm in bulk Si, consuming only 50 nm of the hard mask. Finally, a wet-etching step using Tetra-methyl-ammonium hydroxide (TMAH) is done to form a pillar of a pyramidal shape (Fig. 2(f)). This is required to prevent optical modes circulating the gears from leaking into the bulk Si [43], and to release the pre-stressed BOX and PECVD SiO_2 layers in order to apply tensile strain [19, 26, 29–32, 35–37]. Tuning of this wet-etching step was done by monitoring optical-microscopy (OM) images of SiO_2 micro-disks on Si pillars after being under-etched by TMAH at certain time steps, as shown in Figs. 3(a)-3(f). The tip of the pyramidal Si pillar below the SiO_2 disks can be easily viewed using OM, as SiO_2 is nearly transparent to visible light. Varying the etching time from 10 to 100 minutes, a Si pillar with approximately 500-nm-wide tip was formed after 95-minute etching process, as shown in Fig. 3(f).

3. Results and discussion

3.1. Strain characterization and analysis

Thermal stresses inherent in the BOX and PECVD SiO_2 layers were exploited to induce tensile strain within the Ge structure. Initially, these layers are expected to be compressively stressed [33, 44]. Under-etching the BOX layer upon the formation of the Si pillar using TMAH (Fig. 2(f)) releases the boundaries of the SiO_2 layers. This causes them to expand imposing tensile strain on the encapsulated Ge micro-gear [19, 26, 29–33, 35–37, 44]. Thermally-grown SiO_2 layers, such as the BOX, are expected to have higher initial compressive stresses compared to PECVD SiO_2, due to higher growth temperatures [44]. BOX is usually grown at temperatures around 1000 °C, while PECVD SiO_2 was deposited at 350 °C. Consequently, bearing in mind that the thicknesses of BOX and PECVD layers encapsulating the Ge micro-gears are nearly the same, the bottom BOX layer is expected to impose higher tensile strain on the gears, compared to

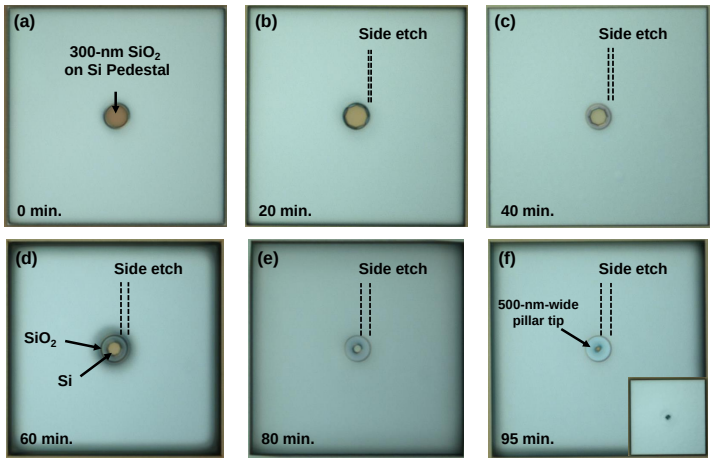

Fig. 3. Tuning of the TMAH wet-etching step to form a Si pillar with approximately 500-nm-wide tip holding the Ge micro-gear on top. The tuning process was done by under-etching 300-nm-thick SiO_2 micro-disks on Si using TMAH and observing the under-etch distance using optical microscopy after (a) zero, (b) 20, (c) 40, (d) 60, (e) 80 and (f) 95 minutes of wet etching. Inset of (f) shows the tip of the Si pillar in focus.

the PECVD layer. This indicates that a strain gradient is expected across the thickness of Ge, being more tensile at the bottom Ge surface.

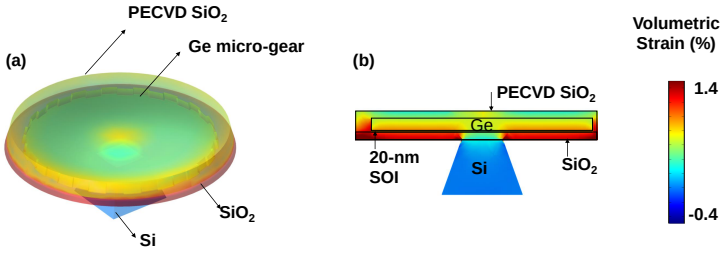

Fig. 4. Finite-element simulation of volumetric strain distribution across a Ge micro-gear on a Si pillar. The micro-gear has an outer diameter of 4 μm, gear depth of 50 nm, and 18 periods. (a) Three-dimensional distribution, and (b) two-dimensional cross-section of the strain in the micro-gear. Higher tensile strain values are expected at the bottom side of the gear compared to the top side due to the higher thermal stresses in the buried SiO_2 (bottom) compared to PECVD SiO_2 (top).

Finite-Element Method (FEM) computer simulations were used to generate a three-dimensional (3D) representation of the strain distribution within the structure. To set up the simulation, initial compressive stresses within the BOX and PECVD SiO_2 layers were allocated as 800 MPA and 250 MPA, respectively. These values were estimated experimentally using Stoney's formula, by measuring the bending radius of a bulk Si wafer with similar SiO_2 layers on top. Ge layer was set to have an initial tensile strain of 0.2% that is inherent in Ge layers grown on Si [27]. The bottom surface of the Si pillar was considered as a fixed boundary. Figure 4(a) shows a 3D distribution of volumetric strain, or the total change in volume, within the structure. According to the strain distribution, the structure is deformed upwards (Fig. 4(a)), as expected due to the

larger initial compressive stresses of BOX, compared to the PECVD. This causes the strain to be slightly non-uniform across the thickness of the Ge micro-gear, as shown in Fig. 4(b). A volumetric tensile strain value of approximately 0.82% (0.6%) is expected at the bottom (top) Ge surface. It is worth mentioning that the corresponding in-plane biaxial tensile strain values are 0.52% and 0.33%, respectively. This lower value of the biaxial tensile strain compared to the volumetric strain is expected, as we neglect the out-of-plane strain component, which is tensile in our case because of the all-around coverage of SiO_2 [32]. This non-uniformity is not preferable from optical point of view, as the overlap between the optical modes and lower-strain regions would impose optical losses rather than optical gain [13, 15, 26, 29–34]. The fact that, non-uniformity of strain is translated into variations of the band-gap [13, 15]. In other words, lower-energy Γ valleys are expected in higher tensile-strained regions [13, 15], increasing the population of electrons and consequently the optical gain within these regions, compared to less tensile-strained regions. However, from carriers point of view, this strain gradient behaves similar to a hetero-junction confining the carriers in the bottom region [45]; where the excited carriers in the top region diffuse towards the bottom region due to its narrower band-gap [13,15,34,45].

On the other hand, the lateral strain distribution is uniform along the radial distance of the micro-gear. For instance, in a micro-gear with an outer radius (R_{out}) of 2 μm, and a gear depth ($R_{out} - R_{in}$) of 50 nm, the strain value along the radial distance is nearly fixed up to 1.7 μm from the center of the gear, at which the strain starts to decay slightly. In the micro-gear shown in Fig. 4(b), the strain value at the bottom surface is approximately 0.82% along the radius, until a radial position of 1.7 μm, where it starts to decay reaching a value of ~0.7% at R_{out} (2 μm). Moreover, the regions in the middle of the Ge micro-gear above the tip of the Si pillar are expected to have low tensile strain values. This is expected as the BOX layer within that region is not released by under-etching, resulting in a negligible expansion (Figs. 4(a) and 4(b)). To ensure an optimum performance of the cavity, whispering gallery modes (WGM) must overlap with the regions of high strain value and uniformity, thus moving away from the gear edges towards the inner regions, yet remaining outside the center of the gear above the Si pillar.

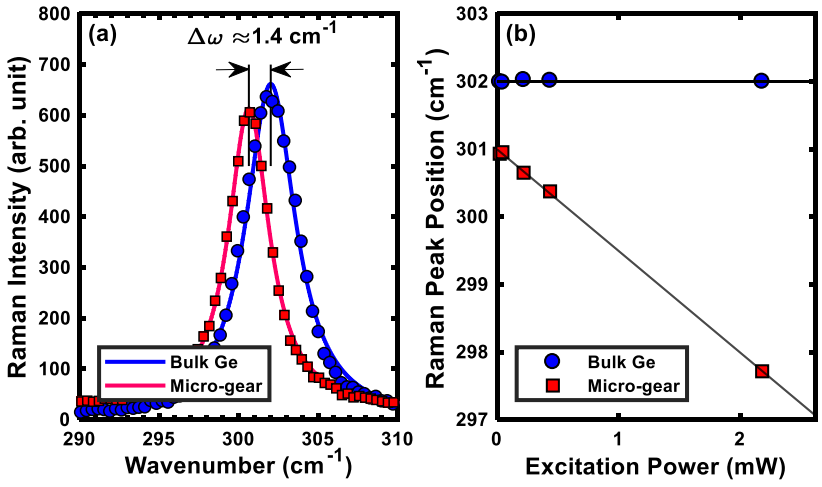

Fig. 5. Raman spectroscopy measurements of Ge micro-gears on Si pillars. (a) Raman spectrum of bulk Ge (blue) and a 4-μm-diameter Ge micro-gear (red) with 18 periods and 50 nm gear depth ($R_{out} - R_{in}$). A Raman shift of 1.4 cm^{-1} is observed at an excitation power of 218 μW. (b) Power dependence of Raman peak position for bulk Ge (blue) and the Ge micro-gear (red). Ge micro-gears are sensitive to heating due to encapsulation with SiO_2.

Confirmation of tensile strain accumulation within Ge was done using Raman spectroscopy. Measurements were done using a 532-nm laser exciting the sample from the top. A power of 218 μW and an exposure time of 5 seconds was used unless indicated otherwise. A 50-times magnification lens was used to collect the Raman signal and direct it to the detector array after being reflected through a 3000 lines/mm grating. Such a high-resolution grating is required to determine the Raman peak position accurately. Each measurement was repeated 10 times and averaged to enhance the signal-to-noise ratio. Raman peaks are fitted by Lorentzian functions in order to estimate the peak position and linewidth. Shift in Raman peak relative to bulk Ge ($\Delta\omega$) is observed in wavenumbers, and accordingly the strain (ϵ) was calculated following the equation: $\Delta\omega = C \times \epsilon$. Where C is a proportionality factor reported in literature to be 390 cm^{-1} for biaxial strain [33–35, 46]. Figure 5(a) shows a sample Raman spectrum for a 4-μm-diameter gear with 18 periods, compared to bulk Ge. The device peak is redshifted with approximately 1.4 cm^{-1} relative to the Bulk Ge Raman peak located around 302 cm^{-1}. The redshift in the Raman spectrum indicates the accumulation of tensile strain [33, 34, 46].

However, heating effects have to be considered in strain measurements using Raman spectroscopy. The fact that the increase in temperature is immediately translated into a redshift in the Raman peak, resulting in an over-estimated strain value [33, 46]. Sensitivity of Raman peak position to heating depends on the device structure and materials. For instance, free standing structures surrounded by air are expected to be extremely sensitive to heating [33, 34, 46]. In our case, Ge micro-gears are fabricated on Si pillars, yet encapsulated with SiO_2. Accordingly, we performed a study on Raman peak position dependence on the excitation power, while fixing all other measurement conditions. Laser power at the surface of the samples was increased from 21.8 μW to 2180 μW. Additional redshift of the Raman peak position was observed upon increasing the power. This dependence is linear within the range of excitation power values used in our experiment. By plotting Raman peak position versus the excitation power (Fig. 5(b)), it is possible to eliminate the effect of heating by extrapolating the linear relation to the limit of negligible excitation power [46]. For example, if we extrapolate the Raman peak-position versus excitation power of the 4-um-diameter micro-gear, the estimated tensile strain value drops to a maximum value of 0.3% after eliminating the heating effect. The slope of this line (Fig. 5(b)) represents the sensitivity of peak position to excitation power given in cm^{-1}/mW. For instance, a power-induced Raman shift of 4.74×10^{-5} cm^{-1}/mW and -1.545 cm^{-1}/mW is found for bulk Ge and a 4-um-diameter micro-gear with 18 periods, respectively. This higher sensitivity to heating compared to bulk Ge is presumably due to the absence of an efficient heat leakage path to the bulk substrate, as the heat conduction path is interrupted by the low-thermal-conductivity SiO_2 [46]. Based on simulation results shown in Fig. 4(b), the bottom Ge micro-gear surface is expected to have higher tensile strain values. Bearing in mind the shallow penetration depth of the 532-nm laser into Ge, estimated in literature to be approximately 20 nm, our Raman measurements represent the less tensile-strained top Ge surface. The increase in the tensile strain moving from the top towards the bottom Ge surface can reach up to 30%, according to simulations (Fig. 4(b)). A better understanding of strain distribution can be formed based on the photo-luminescence results provided in the next section.

3.2. Photo-luminescence and optical modes characteristics

We have studied room temperature photo-luminescence (PL) of Ge micro-gears on Si pillars. Pumping and signal collection was done through a 50-times objective lens from the top. Excitation was done using a continuous wave (CW) laser source with a wavelength of 532 nm. As the excitation power is increased from 0.4 mW to 2 mW, sharp-peak resonances existing within the direct-gap of Ge are observed, as shown in Fig. 6. Modes were detected from Ge micro-gears

with 4 μm outer diameter, 50 nm gear depth and all the fabricated periods ranging from 14 to 21. A sample spectrum is shown in Fig. 6 measured from a micro-gear with 18 periods ($2R_{out}$ = 4μm, $R_{out} - R_{in}$ = 50 nm). The spectrum consists of a broad peak located around ~1.63 μm, and multiple sharp-peak resonances at higher wavelengths. The broad peak can be attributed to Γ-heavy hole (HH) recombinations [13, 15, 33, 34, 46], while the sharp-peak resonant modes are more probably due to Γ-light hole (LH) recombinations [13, 15, 33, 34, 46]. A Γ-HH peak residing around 1.63 μm indicates a biaxial tensile strain value of approximately 0.5% corresponding to the emission [13, 15]. This value is higher than the estimated using Raman spectroscopy; Presumably because the direct-gap PL is mainly originating within the higher tensile-strained Ge regions [13, 15, 26, 29–34, 46], at the bottom surface of the micro-gear. Strain-originated band-gap variations in the same Ge structure generate a hetero-junction-like effect confining the carriers within the higher tensile-strained regions [25, 34, 45, 46]. Consequently, the excited carriers are expected to diffuse from the top surface of the micro-gear upon laser pumping, towards the bottom surface of the micro-gear which has a smaller band gap being more tensile strained [13, 15, 26, 29–34, 46]. While in Raman spectroscopy, the measured strain value represents the top slice of the micro-gear determined by the penetration depth of the pump laser as discussed earlier. This area has the minimum tensile strain value across the Ge thickness (Fig. 4(b)). These two measurements, Raman Spectroscopy and PL, can be combined according to simulations results shown in Fig. 4, by stating that the biaxial tensile strain varies across the thickness of the micro-gear from approximately 0.3% to 0.5% moving from the top to the bottom Ge surfaces. Accordingly, it can be stated that experimental results agree to a good extent with the simulation results presented earlier, indicating that higher tensile strain values are required for more efficient direct-gap emissions.

Finite-Difference Time-Domain (FDTD) simulations were conducted to explore the resonant modes observed at 1.671, 1.728 and 1.787 μm. These resonant modes were identified as transverse-electric (TE) whispering-gallery modes (WGM) [19, 26, 29–33, 37]. TE modes indicate in-plane confinement of the electric field components of the optical wave [33, 43]. Following the annotation of $TE_{\overline{m},n}$ for WGM, these resonant modes can be labeled as $TE_{20,1}$, $TE_{19,1}$ and $TE_{18,1}$, respectively. Where $\overline{m}$ is the number of full wavelengths of the resonant mode circulating the inner circumference of the micro-gear, and n is the total number of field maxima along the radius of the micro-gear [33]. Further investigation of the resonant spectrum using FDTD simulations, we identified the tendency of certain resonances to propagate vertically, or out-of-plane of the micro-gears. Contrary to standard WGMs observed in conventional micro-disks which are emitted radially about the disk plane [47]. This characteristic is presumably due to the gears angular gratings affecting the WGMs as they circulate the inner circumference of the cavity, effectively working as a second-order grating coupler [48]. Vertical emission of the resonant modes in Fig. 6 was confirmed in simulations by multiple methods, such as monitoring the resonant spectrum inside and above the cavity, measuring the optical fields transmitted vertically upwards, and calculating far-field projections. Insets of Fig. 6 plot the absolute and real values, in addition to the phase of the in-plane polar electric field component (E_ρ) travelling upwards as seen at a distance of 2 μm above the gear surface. The insets are labelled as $|E_\rho|$, $\mathrm{Re}(\mathrm{E}_\rho)$ and $\angle(E_\rho)$, respectively. We have also calculated the far-field projections of $TE_{20,1}$, $TE_{19,1}$ and $TE_{18,1}$, as shown in Fig. 7. Far-field calculations represent the electric fields as projected at a hemisphere with a radius of 1 m centered around the device. Azimuthal and polar angles are marked on Fig. 7, indicating the angular distribution and the upwards directionality, respectively. It is noticed that the modes $TE_{20,1}$, $TE_{19,1}$ and $TE_{18,1}$ have a total polar angle spread of 100, 60 and 40 degrees, respectively. Indicating that the higher wavelength mode $TE_{18,1}$ is highly directional compared to $TE_{19,1}$ and $TE_{20,1}$, respectively.

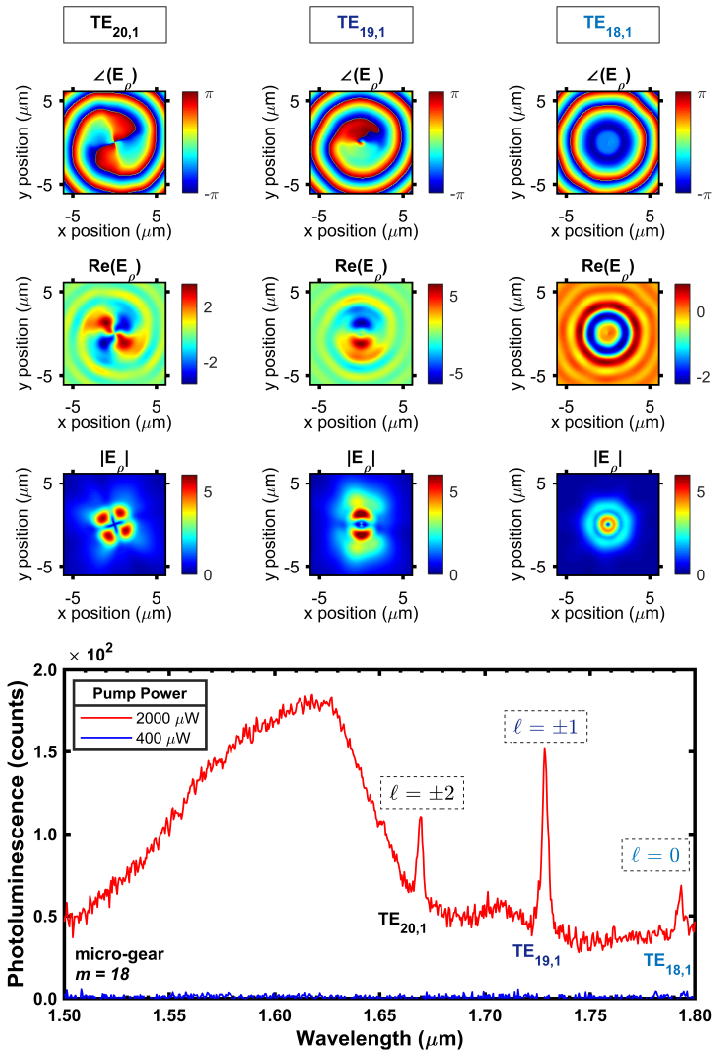

Fig. 6. Photo-luminescence study of a 4-μm-diameter Ge micro-gear (red) with 18 periods and 50 nm gear depth ($R_{out} - R_{in}$). Spectra are experimentally measured by exciting the micro-gear from the top with 0.4 mW and 2 mW laser beams. Sharp peak resonances are observed as the excitation power is increased. Modes at 1.671, 1.728 and 1.787 μm are $TE_{20,1}$, $TE_{19,1}$ and $TE_{18,1}$ whispering gallery modes, respectively. Surface plots on top of the spectra represent the simulated absolute ($|E_\rho|$) and real ($\mathrm{Re}(E_\rho)$) values in addition to the phase ($\angle(E_\rho)$) of the in-plane radial component of the electric field (E_ρ), monitored at a distance of 2 μm above the gear surface. Annular field intensity, and the vortex-shaped wave-front noticed in the real value and phase plots, indicate that $TE_{20,1}$ and $TE_{19,1}$ modes have an orbital angular momentum of 2 and 1, respectively.

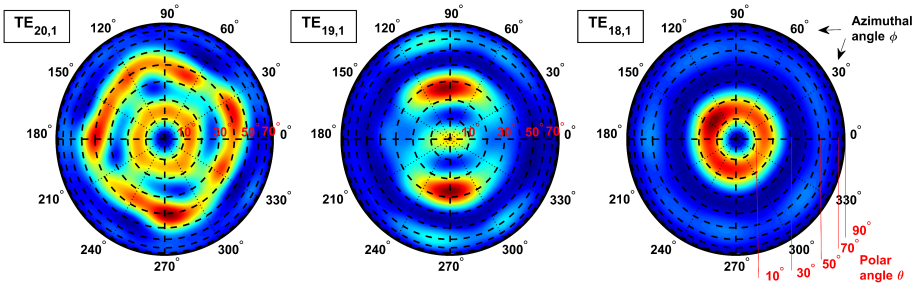

Fig. 7. Far-field projections of the resonant modes $TE_{20,1}$, $TE_{19,1}$ and $TE_{18,1}$. Azimuthal angle represents the in-plane angle around the micro-gear, while the polar angle represents the deviation from the vertical direction (direction [001] in Fig. 1(d)). Polar angle spread of the modes indicates their upwards propagation direction, with the higher wavelength modes being more directional.

Another remarkable characteristic of the modes can be concluded based on the helical nature of the wave-fronts of $TE_{19,1}$ and $TE_{20,1}$, which can be easily spotted in the plots of $Re(E_\rho)$, and more importantly the existence of a phase vortex with a singularity in the middle, as shown in Fig. 6 ($\angle(E_\rho)$) [40,48,49]. The phase singularity results in an annular modal profile as evident in Figs. 6 and 7 ($|E_\rho|$, $Re(E_\rho)$ and far-fields). Accordingly, non-zero orbital angular momentum (ℓ) of 2 and 1 can be assigned to modes at 1.671 and 1.728 μm, respectively [40,48,49]. The fact that, a phase transition from -π to π occurs twice across the wave-front of the mode at 1.671 μm, and once at 1.728 μm. These transitions also reflect on the annular field distributions causing them to have four and two lobes, respectively, as seen in Figs. 6 and 7. Similar phase and intensity distributions are observed for the in-plane azimuthal field component (E_ϕ). Moreover, we have observed the spatial evolution of the modes at higher vertical distances of 4, 4.5 and 5 μm above the micro-gear. This was done by monitoring the phase ($\angle(E_\rho)$) and the real ($Re(E_\rho)$) value of the in-plane field component, as shown in Fig. 8. The phase transition edge marking the jump from $-\pi$ to π is marked with a white dashed arrow, as seen in the phase plots ($\angle(E_\rho)$) in Fig. 8. Considering the direction of the phase transition edge, and the real values of the fields, it is evident that both modes, $TE_{19,1}$ and $TE_{20,1}$, rotate as they propagate in the z direction creating an optical vortex [40,48,49]. By assuming the direction of rotation to be clock-wise or counter clock-wise, these modes can be described by being right or left handed, depending on the direction of the phase transition. For instance, assuming the both modes rotate clock-wise while ascending in the z direction as seen from the top, then they can be labeled as right handed. This definition specifies the sign of the orbital angular momentum number (ℓ) to be positive. As the direction of rotation is not controlled in our structure, degenerate modes are expected to exist at the same wavelengths yet with a reverse direction of rotation or reverse handedness. Optical signals having non-zero OAM, or optical vortices, hold a great potential for multiple applications [40,48–50]. Such as micro-manipulation or optical tweezers, optical microscopy, sensing, and quantum information [48,49]. Moreover, optical signals carrying OAM will have a great impact on optical communications [50]. Offering privileges in terms of reduced cross-talk and boosting data-rates by providing another dimension of multiplexing based on their helical structure [50].

4. Conclusion

We have investigated Ge micro-gears on Si pillars encapsulated within SiO_2 as a source of tensile strain. Characterizing the strain distribution within the device using computer simulations and Raman spectroscopy, we confirmed the accumulation of tensile strain. Tensile strain value

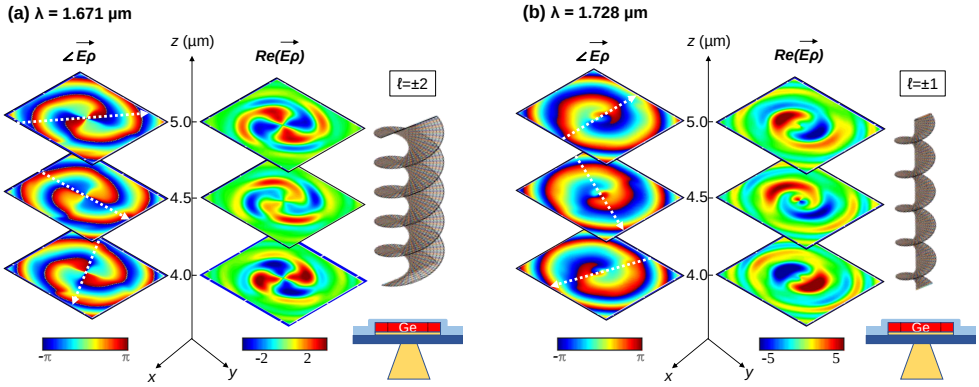

Fig. 8. Spatial evolution of the helical wave-fronts of (a) $TE_{20,1}$ at 1.671 μm, and (b) $TE_{19,1}$ at 1.728 μm. Each plot shows the phase ($\angle(E_\rho)$) and the real ($\mathrm{Re}(E_\rho)$) value of the in-plane polar electric field component (E_ρ) as seen at a distance of 4, 4.5 and 5 μm above the micro-gear surface. Arrows on the phase plots specify the phase transition edge as it changes from $-\pi$ to π. The rotation of the optical vortex for each mode is evident as it propagates upwards. Sketches on the right side of (a) and (b) plot a corresponding schematic of a wave with OAM of 2 and 1, respectively.

varied across the thickness of Ge ranging between 0.3% and 0.5%, as estimated based on Raman spectroscopy and PL measurements. The confinement of sharp-peak WGM was evident in the PL spectra of a micro-gear with 18 periods. In order to understand the effect of the gear boundaries on the optical modes, FDTD simulations were conducted. Tendency of the confined modes to travel vertically upwards was found based on monitoring the confined and emitted spectra, fields at 2 μm distance above the gear surface, and calculating the far-fields. Further investigation of the wave-front intensity and phase distribution, vertically-travelling modes were found to carry non-zero OAM. Optical vortices with 1 and 2 OAM numbers were identified. We believe that Ge micro-gears hold a great potential as a CMOS-compatible OAM light source, considering the emerging applications.

Funding

EPSRC Standard Grant (EP/M009416/1).
EPSRC Manufacturing Fellowship (EP/M008975/1).
EPSRC Platform Grant under Grant (EP/N013247/1).

Acknowledgments

We would like to thank our research collaborators, engineers, and line managers in Hitachi, the University of Tokyo, and University of Southampton for supporting this project. The data in this paper can be obtained from the University of Southampton ePrints research repository: https://doi.org/10.5258/SOTON/D0671.

References

1. S. Saito, F. Y. Gardes, A. Z. Al-Attili, K. Tani, K. Oda, Y. Suwa, T. Ido, Y. Ishikawa, S. Kako, S. Iwamoto, and Y. Arakawa, "Group IV light sources to enable the convergence of photonics and electronics," Front. Mater. **1**, 15 (2014).

2. S. Saito, A. Z. Al-Attili, K. Oda, and Y. Ishikawa, "Towards monolithic integration of germanium light sources on silicon chips," Semicond. Sci. Technol. **31**, 043002 (2016).
3. J. Liu, L. C. Kimerling, and J. Michel, "Monolithic Ge-on-Si lasers for large-scale electronic-photonic integration," Semicond. Sci. Technol. **27**, 094006 (2012).
4. J. Liu, R. Camacho-Aguilera, J. T. Bessette, X. Sun, X. Wang, Y. Cai, L. C. Kimerling, and J. Michel, "Ge-on-Si optoelectronics," Thin Solid Films **520**, 3354–3360 (2012).
5. Z. Zhou, B. Yin, and J. Michel, "On-chip light sources for silicon photonics," Light. Sci. Appl. **4**, e358 (2015).
6. D. A. B. Miller, "Device requirements for optical interconnections to silicon chips," Proc. IEEE **97**, 1166–1185 (2009).
7. G. T. Reed, G. Mashanovich, F. Y. Gardes, and D. J. Thomson, "Silicon optical modulators," Nat. Photon. **4**, 518 (2010).
8. K. Debnath, H. Arimoto, M. K. Husain, A. Prasmusinto, A. Al-Attili, R. Petra, H. M. H. Chong, G. T. Reed, and S. Saito, "Low-loss silicon waveguides and grating couplers fabricated using anisotropic wet etching technique," Front. Mater. **3**, 10 (2016).
9. Y. Ishikawa, K. Wada, J. Liu, D. D. Cannon, H. C. Luan, J. Michel, and L. C. Kimerling, "Strain-induced enhancement of near-infrared absorption in Ge epitaxial layers grown on Si substrate," J. Appl. Phys. **98**, 013501 (2005).
10. X. Wang, H. Li, R. Camacho-Aguilera, Y. Cai, L. C. Kimerling, J. Michel, and J. Liu, "Infrared absorption of n-type tensile-strained Ge-on-Si," Opt. Lett. **38**, 652–654 (2013).
11. J. Michel, J. Liu, and L. C. Kimerling, "High-performance Ge-on-Si photodetectors," Nat. Photon. **4**, 527–534 (2010).
12. D. J. Paul, "Si/SiGe heterostructures: from material and physics to devices and circuits," Semicond. Sci. Technol. **19**, R75 (2004).
13. C. G. V. de Walle, "Band lineups and deformation potentials in the model-solid theory," Phys. Rev. B **39**, 1871 (1989).
14. M. V. Fischetti and S. E. Laux, "Band structure, deformation potentials, and carrier mobility in strained Si, Ge, and SiGe alloys," J. Appl. Phys. **80**, 2234 (1996).
15. M. E. Kurdi, G. Fishman, S. Sauvage, and P. Boucaud, "Band structure and optical gain of tensile-strained germanium based on a 30 band k.p formalism," J. Appl. Phys. **107**, 013710 (2010).
16. X. Sun, J. Liu, L. C. Kimerling, and J. Michel, "Toward a germanium laser for integrated silicon photonics," IEEE J. Sel. Top. Quantum Electron. **16**, 124–131 (2010).
17. B. Dutt, D. S. Sukhdeo, D. Nam, B. M. Vulovic, Z. Yuan, and K. C. Saraswat, "Roadmap to an efficient germanium-on-silicon laser: strain vs. n-type doping," IEEE Photon. J. **4**, 1–9 (2012).
18. A. Z. Al-Attili, S. Kako, M. K. Husain, F. Y. Gardes, H. Arimoto, N. Higashitarumizu, S. Iwamoto, Y. Arakawa, Y. Ishikawa, and S. Saito, "Spin-on doping of germanium-on-insulator wafers for monolithic light sources on silicon," Jpn. J. Appl. Phys. **54**, 052101 (2015).
19. M. E. Kurdi, M. Prost, A. Ghrib, S. Sauvage, X. Checoury, G. Beaudoin, I. Sagnes, G. Picardi, R. Ossikovski, and P. Boucaud, "Direct band gap germanium microdisks obtained with silicon nitride stressor layers," ACS Photon. **3**, 443–448 (2016).
20. J. Liu, X. Sun, L. C. Kimerling, and J. Michel, "Direct-gap optical gain of Ge on Si at room temperature," Opt. Lett. **34**, 1738–1740 (2009).
21. X. Xu, X. Wang, K. Nishida, K. Takabayashi, K. Sawano, Y. Shiraki, H. Li, J. Liu, and T. Maruizumi, "Ultralarge transient optical gain from tensile-strained, n-doped germanium on silicon by spin-on dopant diffusion," Appl. Phys. Express **8**, 092101 (2015).
22. J. Liu, X. Sun, R. Camacho-Aguilera, L. C. Kimerling, and J. Michel, "Ge-on-Si laser operating at room temperature," Opt. Lett. **35**, 679–681 (2010).
23. R. Koerner, M. Oehme, M. Gollhofer, M. Schmid, K. Kostecki, S. Bechler, D. Widmann, E. Kasper, and J. Schulze, "Electrically pumped lasing from Ge fabry-perot resonators on Si," Opt. Express **23**, 14815–14822 (2015).
24. R. E. Camacho-Aguilera, Y. Cai, N. Patel, J. T. Bessette, M. Romagnoli, L. C. Kimerling, and J. Michel, "An electrically pumped germanium laser," Opt. Express **20**, 11316–11320 (2012).
25. S. Bao, D. Kim, C. Onwukaeme, S. Gupta, K. Saraswat, K. H. Lee, Y. Kim, D. Min, Y. Jung, H. Qiu, H. Wang, C. S. T. E. A. Fitzgerald, and D. Nam, "Low-threshold optically pumped lasing in highly strained germanium nanowires," Nat. Commun. **8**, 1845 (2017).
26. A. Elbaz, M. E. Kurdi, A. Aassime, S. Sauvage, X. Checoury, I. Sagnes, C. Baudot, F. Boeuf, and P. Boucaud, "Germanium microlasers on metallic pedestals," APL Photon. **3**, 106102 (2018).
27. Y. Ishikawa, K. Wada, D. D. Cannon, J. Liu, H. C. Luan, and L. C. Kimerling, "Strain-induced band gap shrinkage in Ge grown on Si substrate," Appl. Phys. Lett. **82**, 2044 (2003).
28. C. Ortolland, Y. Okuno, P. Verheyen, C. Kerner, C. Stapelmann, M. Aoulaiche, N. Horiguchi, and T. Hoffmann, "Stress memorization technique—fundamental understanding and low-cost integration for advanced CMOS technology using a nonselective process," IEEE Trans. Electron Devices **56**, 1690–1697 (2009).
29. A. Ghrib, M. de Kersauson, M. E. Kurdi, R. Jakomin, G. Beaudoin, S. Sauvage, G. Fishman, G. Ndong, M. Chaigneau, R. Ossikovski, I. Sagnes, and P. Boucaud, "Control of tensile strain in germanium waveguides through silicon nitride layers," Appl. Phys. Lett. **100**, 201104 (2012).
30. A. Ghrib, M. E. Kurdi, M. de Kersauson, M. Prost, S. Sauvage, X. Checoury, G. Beaudoin, I. Sagnes, and P. Boucaud, "Tensile-strained germanium microdisks," Appl. Phys. Lett. **102**, 221112 (2013).
31. A. Ghrib, M. E. Kurdi, M. Prost, M. de Kersauson, L. Largeau, O. Mauguin, G. Beaudoin, S. Sauvage, X. Checoury,

G. Ndong, M. Chaigneau, R. Ossikovski, S. David, I. Sagnes, and P. Boucaud, "Strain engineering in germanium microdisks," Proc. SPIE 8990, Silicon Photonics IX, p. 89901C (2014).
32. A. Ghrib, M. E. Kurdi, M. Prost, S. Sauvage, X. Checoury, G. Beaudoin, M. Chaigneau, R. Ossikovski, I. Sagnes, and P. Boucaud, "All-around SiN stressor for high and homogeneous tensile strain in germanium microdisk cavities," Adv. Opt. Mater. **3**, 353–358 (2015).
33. A. Z. Al-Attili, S. Kako, M. Husain, F. Gardes, N. Higashitarumizu, S. Iwamoto, Y. Arakawa, Y. Ishikawa, H. Arimoto, K. Oda, T. Ido, and S. Saito, "Whispering gallery mode resonances from Ge micro-disks on suspended beams," Front. Mater. **2**, 43 (2015).
34. D. Burt, A. Al-Attili, Z. Li, F. Gardès, M. Sotto, N. Higashitarumizu, Y. Ishikawa, K. Oda, O. M. Querin, S. Saito, and R. Kelsall, "Enhanced light emission from improved homogeneity in biaxially suspended germanium membranes from curvature optimization," Opt. Express **25**, 22911–22922 (2017).
35. G. Capellini, C. Reich, S. Guha, Y. Yamamoto, M. Lisker, M. Virgilio, A. Ghrib, M. E. Kurdi, P. Boucaud, B. Tillack, and T. Schroeder, "Tensile Ge microstructures for lasing fabricated by means of a silicon complementary metal-oxide-semiconductor process," Opt. Express **22**, 399–410 (2014).
36. R. W. Millar, K. Gallacher, A. Samarelli, J. Frigerio, D. Chrastina, G. Isella, T. Dieing, and D. J. Paul, "Extending the emission wavelength of Ge nanopillars to 2.25 μm using silicon nitride stressors," Opt. Express **23**, 18193–18202 (2015).
37. R. W. Millar, K. Gallacher, J. Frigerio, A. Ballabio, A. Bashir, I. MacLaren, G. Isella, and D. J. Paul, "Analysis of Ge micro-cavities with in-plane tensile strains above 2%," Opt. Express **24**, 4365–4374 (2016).
38. R. Dangel, J. Hofrichter, F. Horst, D. Jubin, A. L. Porta, N. Meier, I. M. Soganci, J. Weiss, and B. J. Offrein, "Polymer waveguides for electro-optical integration in data centers and high-performance computers," Opt. Express **23**, 4736–4750 (2015).
39. D. Taillaert, F. V. Laere, M. Ayre, W. Bogaerts, D. V. Thourhout, P. Bienstman, and R. Baets, "Grating couplers for coupling between optical fibers and nanophotonic waveguides," Jpn. J. Appl. Phys. **45**, 6071 (2006).
40. H. Li, D. B. Phillips, X. Wang, Y.-L. D. Ho, L. Chen, X. Zhou, J. Zhu, S. Yu, and X. Cai, "Orbital angular momentum vertical-cavity surface-emitting lasers," Optica **2**, 547–552 (2015).
41. M. Fujita and T. Baba, "Microgear laser," Appl. phys. lett. **80**, 2051–2053 (2002).
42. K. Nozaki, A. Nakagawa, D. Sano, and T. Baba, "Ultralow threshold and single-mode lasing in microgear lasers and its fusion with quasi-periodic photonic crystals," IEEE J. Sel. Top. Quantum Electron. **9**, 1355–1360 (2003).
43. S. L. Chuang, *Physics of Photonic Devices*, vol. 80 (John Wiley & Sons, 2012).
44. S. D. Senturia, *Microsystem Design* (Kluwer academic publishers, Boston, 2001).
45. D. Nam, D. S. Sukhdeo, J. H. Kang, J. Petykiewicz, J. H. Lee, W. S. Jung, J. Vučković, M. L. Brongersma, and K. C. Saraswat, "Strain-induced pseudoheterostructure nanowires confining carriers at room temperature with nanoscale-tunable band profiles," Nano Lett. **13**, 3118–3123 (2013).
46. A. Z. Al-Attili, S. Kako, M. K. Husain, F. Y. Gardes, S. Iwamoto, Y. Arakawa, and S. Saito, "Tensile strain engineering of germanium micro-disks on free-standing SiO_2 beams," Jpn. J. Appl. Phys. **55**, 04EH02 (2016).
47. S. L. McCall, A. F. J. Levi, R. E. Slusher, S. J. Pearton, and R. A. Logan, "Whispering gallery mode microdisk lasers," Appl. Phys. Lett. **60**, 289–291 (1992).
48. X. Cai, J. Wang, M. J. Strain, B. Johnson-Morris, J. Zhu, M. Sorel, J. L. O'Brien, M. G. Thompson, and S. Yu, "Integrated compact optical vortex beam emitters," Science **338**, 363–366 (2012).
49. H. Rubinsztein-Dunlop, A. Forbes, M. V. Berry, M. R. Dennis, D. L. Andrews, M. Mansuripur, C. Denz, C. Alpmann, P. Banzer, T. Bauer, E. Karimi, L. Marrucci, M. Padgett, M. Ritsch-Marte, N. M. Litchinitser, N. P. Bigelow, C. Rosales-GuzmÃąn, A. Belmonte, J. P. Torres, T. W. Neely, M. Baker, R. Gordon, A. B. Stilgoe, J. Romero, A. G. White, R. Fickler, A. E. Willner, G. Xie, B. McMorran, and A. M. Weiner, "Roadmap on structured light," J. Opt. **19**, 013001 (2016).
50. A. E. Willner, H. Huang, Y. Yan, Y. Ren, N. Ahmed, G. Xie, C. Bao, L. Li, Y. Cao, Z. Zhao, J. Wang, M. P. J. Lavery, M. Tur, S. Ramachandran, A. F. Molisch, N. Ashrafi, and S. Ashrafi, "Optical communications using orbital angular momentum beams," Adv. Opt. Photon. **7**, 66–106 (2015).